An Automated Method to Analyze Tropical Cyclone Surface Winds from Real-Time Aircraft Reconnaissance Observations

JOHN A. KNAFF[a] AND CHRISTOPHER J. SLOCUM[a]

[a] *Center for Satellite Applications and Research, NOAA, Fort Collins, Colorado*

(Manuscript received 8 May 2023, in final form 5 December 2023, accepted 5 December 2023)

ABSTRACT: This study describes an automated analysis of real-time tropical cyclone (TC) aircraft reconnaissance observations to estimate TC surface winds. The wind analysis uses an iterative, objective, data-weighted analysis approach with different smoothing constraints in the radial and azimuthal directions. Smoothing constraints penalize the data misfit when the solutions deviate from smoothed analyses and extend the aircraft information into areas not directly observed. The analysis composites observations following storm motion taken within 5 h prior and 3 h after analysis time and makes use of prescribed methods to move observations to a common flight level (CFL; 700 hPa) for analysis and to reduce reconnaissance observations to the surface. Comparing analyses to several observed and simulated wind fields shows that analyses fit the observations while extending observational information to poorly observed regions. However, resulting analyses tend toward greater symmetry as observational coverage decreases, and show sensitivity to the first guess information in unobserved radii. Analyses produce reasonable and useful estimates of operationally important characteristics of the wind field. But, due to the radial and azimuthal smoothing and the undersampling of typical aircraft reconnaissance flights, wind maxima are underestimated, and the radii of maximum wind are slightly overestimated. Varying observational coverage using model-based synthetic aircraft observations, these analyses improve as observational coverage increases, and for a typical observational pattern (two transects through the storm) the root-mean-square error deviation is <10 kt (<5 m s^{-1}).

SIGNIFICANCE STATEMENT: Many applications need estimates of 2D surface winds in tropical cyclones in real time. While real-time aircraft-based observations of the winds inside tropical cyclones have been available for several decades, there have been few automated and objective methods to analyze this information to provide estimates of the strength and distribution of the surface winds. Here, we provide details of one method that fuses these unique observations to provide useful 2D analyses of the winds in and around tropical cyclones.

KEYWORDS: Tropical cyclones; Wind; Aircraft observations; Variational analysis

1. Introduction

Aircraft reconnaissance provides routine in-storm tropical cyclone (TC) observations in the North Atlantic and eastern North Pacific for the operational and research communities. Since the mid-1990s, aircraft reconnaissance has disseminated flight-level and Stepped Frequency Microwave Radiometer [SFMR; Uhlhorn et al. (2007) and references therein] observations in real time via a standardized format known as High Density Observations (HDOBS). Despite the real-time availability of these observations, few tools exist to analyze these winds and even fewer tools to create analyses or estimates of the 2D surface wind field.

One method, the Hurricane Research Division H*Wind system, combines reconnaissance surface station, ship, and buoy observations, and satellite-derived atmospheric motion vectors. The H*Wind system composites these observations in a storm-following framework over a period, to estimate the 1-min sustained 10-m level wind with appropriate adjustments for the wind averaging period and height (Powell et al. 1998). Because of these steps, H*Wind generates a sophisticated and robust surface wind analysis (Powell et al. 2010). The National Hurricane Center (NHC) assessed the H*Wind system for suitability in operations as part of the Joint Hurricane Testbed (JHT; Rappaport et al. 2012). Unfortunately, H*Wind never became an operational product. Since then, the H*Wind system and its analyses became proprietary, but remain available for research applications.

In 2011, Knaff et al. developed a simple automated, objective algorithm to estimate and analyze the surface wind field from aircraft reconnaissance observations via the HDOBS as a JHT project. The algorithm extends from a satellite-only TC surface wind analysis as described in Knaff et al. (2011). The algorithm also attempts to loosely follow some operational practices while accommodating other suggestions from the literature for the treatment of SFMR-based surface winds and the reduction of flight-level winds to the 10-m marine exposure. The original Knaff et al. (2011) algorithm was adapted to use that combination of the 2012–14 guidelines for input observation treatment. Note that these guidelines change as research and operations glean new insight. JHT recommended the algorithm for operational implementation in 2014, but a transition to operations did not occur. However, the development of

Supplemental information related to this paper is available at the Journals Online website: https://doi.org/10.1175/WAF-D-23-0077.s1.

Corresponding author: John Knaff, John.Knaff@noaa.gov

DOI: 10.1175/WAF-D-23-0077.1

an updated fitting algorithm and public dissemination and sharing[1,2] of real-time TC surface wind analyses continued.

Despite lacking formal documentation, these wind analyses are used for application development, validation of surface wind fields, estimation of the radius of maximum winds, and in several studies (e.g., Mouche et al. 2019; Nolan et al. 2021). Therefore, the manuscript's purpose is to document the development and formulation of this real-time automated TC surface wind analysis. Section 2 describes the observations used to make these analyses and their treatment, and section 3 describes the methods used to analyze those observations. Section 4 provides performance information including how well the observations fit, sensitivity to observational coverage, and a few comparisons with independent surface wind observations (more in the online supplemental material). The last section provides a summary and discussion of future work.

2. Observations and their horizontal and vertical adjustments

The U.S. Air Force and NOAA weather reconnaissance aircraft HDOBS include the observation time, latitude, longitude, aircraft static air pressure (ASP), aircraft geopotential height, extrapolated surface pressure (APS $\geq$ 550 hPa) or D-value (APS $<$ 550 hPa), sign of the temperature, air temperature, dewpoint temperature, wind direction, wind speed, peak overwater 10-s surface wind speed, rain rate, and quality flags. HDOBS typically have 30-s frequencies. All quantities except the peak surface winds and rain rate are 30-s averages sampled $\pm$15 s of the observation time. The peak surface wind and rain rate based on the SFMR is also sampled $\pm$15 s of the observation time. The SFMR algorithm has been in use since 2016 (Klotz and Uhlhorn 2014). And the HDOBS format is provided in appendix G of the National Hurricane Operations Plan (2022; https://www.weather.gov/media/nws/IHC2022/2022_NHOP_June_1.pdf).

In incorporating the HDOBS, the analysis discussed in section 3 uses the location (latitude and longitude), time, ASP, flight-level winds, and peak SFMR surface wind speeds. In addition to HDOBS, and to provide the recent track of the storm, we use observed times and center locations, hereafter referred to as "fixes," working best tracks, and forecasts. These observations and forecasts come from the real-time databases of the Automated Tropical Cyclone Forecast system (ATCF; Sampson and Schrader 2000). Specifically, the aircraft-based, (i.e., "AIRC") and radar-based (i.e., "RADR") fixes, the working best track, and the interpolated version of the most recent official forecast (i.e., "OFCI"), are used to construct a short-term storm track from 24 h before to 12 h after the analysis time. Table 1 provides an example track for Hurricane Ian (2022) for a 0600 UTC 27 September analysis and all the nonsynoptic times provided by the "AIRC" center fix locations. The HDOBS and fixes come from both Air Force (AF301) and NOAA (NOAA9) aircraft.

[1] http://rammb-data.cira.colostate.edu/products/tc_realtime/.
[2] ftp://rammftp.cira.colostate.edu/knaff/JHT_TCSWA/.

TABLE 1. Example of the short-term track created from the combination of the working best track information, the 12-h forecast position, and the aircraft-based (and radar-based, when available) center fixes for Hurricane Ian at 0600 UTC 27 Sep 2022. Columns provide date, time, and the latitude and longitude of the fix/track/forecast, and in this case, there are 20 track points extracted. The working best track locations are shown in normal text, aircraft fix locations are shown in boldface, and the 12-h forecast location (OFCI) is shown in italics.

Date	Time (UTC)	Lat (°)	Lon (°)
26 Sep 2022	0600	17.70	−81.70
26 Sep 2022	**0615**	**17.76**	**−81.76**
26 Sep 2022	**0718**	**17.99**	**−81.87**
26 Sep 2022	**1011**	**18.41**	**−82.13**
26 Sep 2022	**1125**	**18.63**	**−82.35**
26 Sep 2022	**1139**	**18.65**	**−82.43**
26 Sep 2022	1200	18.70	−82.40
26 Sep 2022	**1244**	**18.79**	**−82.48**
26 Sep 2022	**1308**	**18.87**	**−82.42**
26 Sep 2022	**1453**	**19.18**	**−82.68**
26 Sep 2022	**1632**	**19.53**	**−82.90**
26 Sep 2022	1800	19.70	−83.00
26 Sep 2022	**2203**	**20.35**	**−83.28**
26 Sep 2022	**2321**	**20.71**	**−83.32**
27 Sep 2022	0000	20.80	−83.30
27 Sep 2022	**0102**	**21.02**	**−83.39**
27 Sep 2022	**0241**	**21.29**	**−83.56**
27 Sep 2022	**0356**	**21.38**	**−83.66**
27 Sep 2022	0600	21.80	−83.60
27 Sep 2022	*1800*	*24.40*	*−83.50*

Analyses are created for synoptic times of 0000, 0600, 1200, and 1800 UTC. The observations are aligned in a storm motion-relative framework using the short-term track information. Observations are composited relative to the location of the storm and the observation time (Cline 1920) with the assumption that TC structure and intensity change slowly during collection.[3] The time window for compositing is up to 5 h backward and 3 h forward. In real time, the analysis is run 50 min after the synoptic time and then again 2 h, 50 min after the synoptic time. So, the analyses are available for operational consideration at the National Hurricane Center near the beginning and again near the end of the advisory process. Table 1 provides an example short-term track for Hurricane Ian that the algorithm uses to estimate the tropical cyclone center position near the end of the operational advisory process. Thus, the windows are roughly 6 and 8 h for the interim and final analyses but often only capture 3–4 h of observations. Cubic splines under tension are used to perform the interpolation of latitude and longitude as a function of time.

[3] In rare instances, the 6-hourly intensity can change 25 kt with corresponding structure variations [e.g., Hurricanes Patricia (2015), Delta (2020)]. However, using best track data interpolated to fix times 2004–22, 96% of the fix intensities are within $\pm$10 kt of the 8-h average intensity, and 85% of the 34-kt winds are within $\pm$10 n mi of the 8-h average 34-kt wind radii. For the 34-kt wind radii comparisons, the average 34-kt wind radii average is the average of all nonzero quadrant values in the TC's final best track.

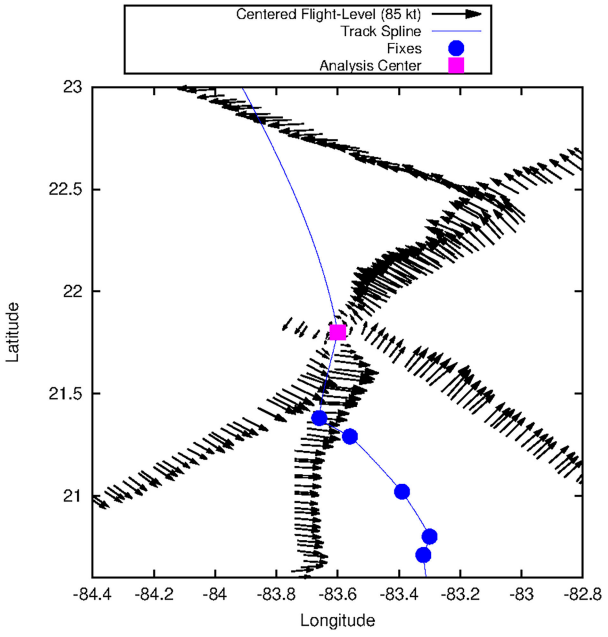

FIG. 1. Fixes (blue dots), analysis center (magenta square), the splined track plotted every 2 min (thin blue line), and the storm-motion relative flight-level winds (kt) adjusted to 700 hPa available for the analysis (vectors). This example is from Hurricane Ian (2022) created shortly after 0600 UTC 27 Sep.

Fitting time versus latitude–longitude pairs (knots) to a cubic spline using software (Press et al. 1992) allows estimates of these quantities within the time interval, and thus the position of the storm at the observation times. In our formulation, we added a constant tension term $T = 0.3$ that multiplies the second derivative terms in each knot interval (note: traditionally, tension in splines is a reciprocal of our T, as in De Boor 1978). This restrains the amount of nonlinear behavior between knots that occasionally produce undesired interpolation when using real observations with variable temporal spacing. Figure 1 shows the details of the resulting track used to relocate aircraft observations for the Hurricane Ian example using the short-term track information and the resulting storm motion-relative observations and locations.

For guidance, we use a combination of suggested treatments of these observations (Franklin et al. 2003; Powell et al. 2009; Uhlhorn and Black 2003), operational practices (e.g., Brennan 2019), and physical justifications (Kepert 2001; Kepert and Wang 2001; Holthuijsen et al. 2012). As in Franklin et al. (2003), we divide the storm into an eyewall and outer region for flight-level to vary surface reduction factors (R). The values we use for R for eyewall and outer regions and different broad pressure layers are shown in Table 2. These values are more conservative than those recommended by Franklin et al. (2003) for estimating the storm's maximum sustained 1-min winds from flight levels. Partial motivation for these choices comes from slightly lower estimates in R discussed in Powell et al. (2009). The pressure-layer-based values of R also allow for adjusting winds to any of these layers and the surface.

TABLE 2. Maximum pressure/flight-level to surface wind reduction factors for eyewall and outer regions of the TC.

Level (hPa)	Eyewall (R_{ew})	Outer vortex (R_o)
600–800	0.88	0.83
800–900	0.78	0.78
900–990	0.73	0.73
990-Sfc	0.77	0.77

We define the eyewall region as the areas inside the smaller of twice the RMW or RMW plus 20 nautical miles (n mi; 1 n mi = 1.852 km) and the outer region as 4 times the RMW. Defining the outer region at a greater radial distance results in a transition zone of R between the eyewall region and outer region, rather than an abrupt change implied in Franklin et al. (2003). In this transition zone, we decided to linearly interpolate R between the eyewall and outer regions, which addresses the uncertainties in these RMW-based regions.

In addition to the radial variations of R, the eyewall region and outer regions vary azimuthally by 4% (Franklin et al. 2003) (i.e., from 0.88 to 0.85 at 700 hPa) and 17% (i.e., from 0.83 to 0.69 at 700 hPa), respectively. The minima of R are located right of TC motion, which is supported by SFMR-dropwindsonde surface wind studies (Powell et al. 2009; Uhlhorn and Black 2003), and by Brennan (2019, slide 14) who suggests a 20% difference from left (0.75) to right (0.90). This outer asymmetry in R is meant to account for the effect of larger drag coefficients left of motion caused by wave orientation discussed in Holthuijsen et al. (2012) and effects related to boundary layer jets (Kepert 2001; Kepert and Wang 2001).

Figure 2 shows how these factors vary spatially for 700 hPa to surface R values for two RMW values, namely, 5.4 and 27 n mi (i.e., 10 and 50 km) with the TC moving toward the top of the page. The occurrence of 5.4 n mi RMW is rare, while 27 n mi RMW features are common (Schwerdt et al. 1979; Willoughby and Rahn 2004; Knaff et al. 2015; Klotz and Jiang 2017; Combot et al. 2020). Thus, in the application, the RMW determines the radial distribution of R, and spatial differences can be quite large as shown in these two examples. Note that as the analysis runs, the RMW can change, and the reduction factors are dynamic throughout the analysis process, described in section 3. Again, note that these observation treatments can be changed if new observations or updated studies develop improved methods for performing a simple flight-level to surface wind reduction (e.g., Kepert 2023).

Prior to running the first objective analysis, we move observations collected in our time window to a common time (i.e., the analysis time). Then, wind speeds and wind components are adjusted to a common 700-hPa flight level or common flight level (CFL) for further analysis as described in section 3.

Finally, to speed up algorithm convergence, the analysis scheme uses a satellite-based first guess provided by the NESDIS operational version of the Multi-satellite-platform

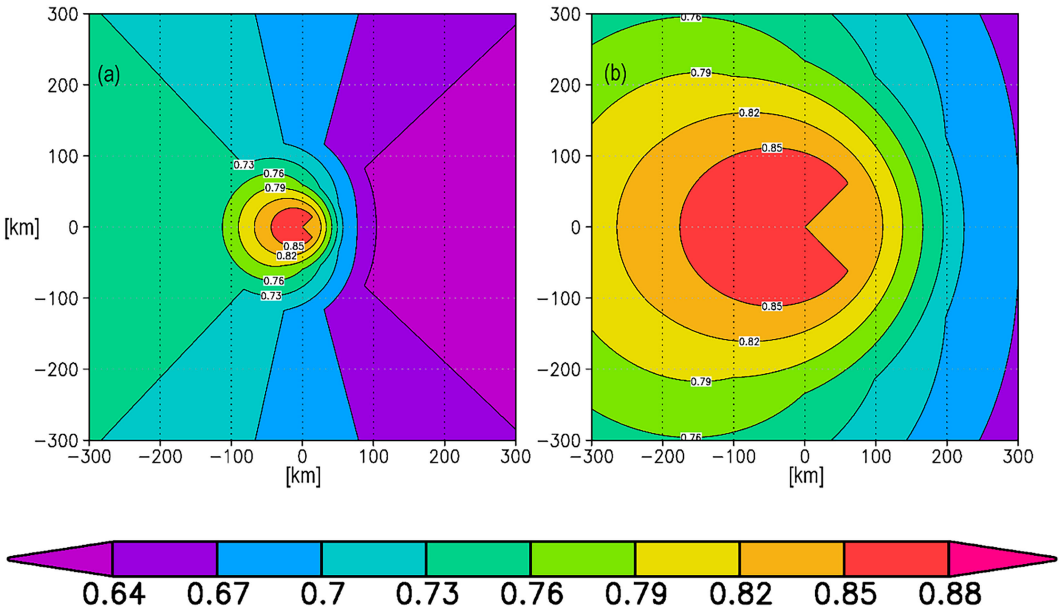

FIG. 2. Example of the 700 hPa to surface reduction factors as a function of radius of maximum wind. Shown are reduction factors (R) for RMW values of (a) 5.4 n mi or 10 km, and (b) 27 n mi or 50 km. Storm motion is toward the top of the page.

Tropical Cyclone Surface Wind Analysis (MTCSWA; Knaff et al. 2011). The first guess is at the 700-hPa level and is the intermediate wind analysis, performed above the influence of surface friction. Without MTCSWA, a Rankine vortex using the maximum observed wind speed and a 50-km radius of maximum wind (RMW) provides a first guess wind field.

3. Analysis methods

With the typical pattern of aircraft observations (figure four or alpha patterns) and the general circular geometry of TCs, we use an appropriate analysis strategy. Our analysis method uses an iterative, objective, data-weighted analysis approach based upon a model-fitting method with directional smoothness constraints termed "variational formalism with smoothing constraints" in Thacker (1988). This method allows input observations to be weighted by taking into account for different types or quality of observations (Mueller et al. 2006) and an iterative solution created via the method of gradient or steepest descent. The analysis counterpart of the observations is estimated using bilinear interpolation to the observation location (Mueller et al. 2006; Knaff et al. 2011). Prescribed smoothing constraints in radial and azimuthal directions allow for the creation of a smoothed analysis termed the "model counterpart" that filters the influence of observations in those directions. Following Mueller et al. (2006), a cost function (1) minimizes the differences between the data misfit that penalized for departures from the model counterpart. In (1) there are k observations with weights w_k, and i and j are polar grid indices. The data misfit is the first term in (1), where the analysis at the observation locations is given by U_k. The second term is the smoothness penalty, where δ_{rr} and $\delta_{\theta\theta}$ are the first order discretized second derivative in radial and azimuthal directions, Uij is the gridded analysis, and α and β are the smoothing constraints:

$$C = \frac{1}{2}\sum_{k=1}^{k} w_k(u_k - U_k)^2 + \sum_{i=1}^{I}\sum_{j=1}^{J}[\alpha(\delta_{rr}U_{ij})^2 + \beta(\delta_{\theta\theta}U_{ij})^2]. \quad (1)$$

Mueller et al. (2006) provides a description of the smoothing constraints in terms of a frequency response function to a pure cosine wave with wavenumber k. They discuss how for a $2\Delta r$ wave on the analysis grid ($k = 2\pi/2\Delta r$), the amplitude will be reduced by a factor of $(1 + 32\alpha)^{-1}$. For (1), α and β are chosen by half-power distances in radial and azimuthal directions. Readers are referred to Mueller et al. (2006) and DeMaria and Jones (1993) for more explanation. For this work, the polar grid has 301 radial points ($\Delta r = 2.0$ km) from $r = 1$ to 601 km and 36 azimuthal points ($\Delta\theta = 10°$), and the wind components are input as radial and tangential values.

For analysis of aircraft-based observations, data weights (w_k) are assigned by wind type (aircraft versus SFMR) and observed aircraft-based wind speeds. The nominal/average data weight is $w = 1.0$. SFMR wind speed data weights are 4 times larger ($w = 4.0$) when flight-level winds exceed 75 kt (38.6 m s^{-1}; 1 kt $\approx$ 0.51 m s^{-1}) and are 3 times smaller ($w = 0.33$) for flight-level winds below 50 kt, and linearly interpolated between those wind speed thresholds. Similarly, flight-level wind vector weights are given 4 times more weight and 3 times less weight when the winds are below 50 kt and above 75 kt, and weights are linearly interpolated between those thresholds. These choices give SFMR more weight for

the most intense wind speeds,[4] and this choice is justified by Nordberg et al. (1971) who showed SFMR senses the sea state best above wind speeds of 30–40 kt (15–20 m s^{-1}). More recently, Sapp et al. (2019) note highly questionable wind speeds below 30 kt and less sensitivity to rainfall's effects above 40 kt. For operational users, Brennan (2019) summarizes the SFMR issues by stating, "Rain impacts not always properly accounted for (mainly <50 kt)." Furthermore, Sapp et al. (2019) provide an independent validation of the current SFMR algorithm with respect to rain rate and add support for our weighting strategy. Again, the data weighting strategy can be changed, noting the ongoing efforts to update the SFMR algorithms (Sapp et al. 2019; H. Holbach 2021, 2023, personal communication).

Since SFMR observations provide only a speed, the wind components and wind speeds are analyzed separately. Once the wind components (radial and tangential) and wind speeds are adjusted to the CFL, the gridpoint wind components are changed. This step ensures that the component-based wind speed is identical to the separate pure wind speed analysis. That is, we treat the pure speed-only analysis that contains aircraft and SFMR inputs as truth. We calculate speed based on the analyses of the radial and tangential winds at every grid point, and a ratio between the pure wind speed analysis and the component-based wind speed analysis is applied to each component at each grid point. This readjustment occurs following each of the five analysis steps as described next.

The objective analysis is run four times, which allows for some additional quality control and smoothing constraint refinement. Figure 3 shows these steps. Before each analysis runs, the original observations are readjusted to the CFL as the observed RMW and Rs often change. This is a two-way iterative process whereby between each of the separate analyses' winds are adjusted from the CFL back to the original pressure using recent values of R, then back to the CFL using the updated values of R as the analyzed RMW changes. The first analysis uses a first guess (data weights are $w = 0.2$) coming from the MTCSWA product (Knaff et al. 2011) or a prescribed Rankine vortex described above if MTCSWA is unavailable. The Rankine vortex is used less than 1% of the time. This first guess weighting strategy follows that of Knaff et al. (2011). For the adjustment of winds to CFL, a value of 50 km is assigned to the initial RMW. The smoothing constraints in the radial direction (α) and in the azimuthal direction (β) are fixed with half powers of 28.8 km and 360° (i.e., data at 14.4 km and 360° receives half the weighting)—a smooth domain-filling first analysis that is symmetric with respect to azimuth. After the first analysis, the first guess data weights are reduced to $w = 0.05$. For the next two analyses, half powers are reduced to $\alpha = 11.2$ km and $\beta = 200°$ and then to $\alpha = 6.4$ km and $\beta = 150°$, respectively. In rare instances, a gross quality control removes observations with absolute errors larger than either 30 m s^{-1} or 30% of the maximum analyzed wind speed following the second analyses, setting those errant data's weights to zero. In the final analysis, the first guess data weights are reduced further to $w = 0.013$, and half powers of $\alpha = 4.8$ km, and $\beta = 120°$ are assigned. As a final step, the wind speed errors between the analysis and observations at the CFL are analyzed using $\alpha = 6.4$ km and $\beta = 150°$ and data weights of $w = 1.0$. Analyzed errors are then added back into the final CFL analysis, and the wind components speed is adjusted one last time. This step is like the second pass of a Barnes (1964) analysis and leads to greater fidelity with reduced computation (Koch et al. 1983). We call this analysis of CLF observations the Objective Iterative method Utilizing Smoothing (OBITUS) analysis hereafter.

Surface type is then determined using a land mask. If located over water, analyzed CFL winds are reduced to a 10-m marine exposure using final estimates of R at the CFL, and inflow angles applied (Zhang and Uhlhorn 2012). Following Knaff et al. (2011) and Boose et al. (2001), wind speeds over land are reduced an additional 20% and inflow angles increased an additional 20° from the marine exposure inflow. Distance to land uses an algorithm briefly described in Merrill (1987) and used in intensity forecasting models (e.g., DeMaria and Kaplan 1999) with coastlines of continents and select islands with a rough resolution of 30 km. Finally, zonal and meridional winds are bilinearly interpolated to a 0.05° × 0.05° Cartesian grid for display purposes and other uses.

4. Performance

The OBITUS analysis discussed above stretches the input observations to fill the observation-void regions and then adds observation-based details by successive reanalyses with weaker filtering. However, because of TC structure as well as the typical observation sampling, smoothing is much greater in azimuthal versus radial directions. This combination of filters, while necessary to stretch observational information to the observation-void regions of the storm, has the greatest impact in regions where wind gradients are the largest—resulting in underestimates of extremes. To assess the performance of these analyses, we first present the bulk statistics of the fit of SFMR and flight-level observations from all cases adjusted to the CFL. A sensitivity analysis based on synthetic aircraft observations extracted from 3D model fields and comparisons with the 3D model's surface wind field then follows. We then present analyses with comparisons to independent synthetic aperture radar (SAR)-based wind speeds (Mouche et al. 2017).

a. Bulk statistics of the fit with respect to wind speed

One of the goals of this analysis is to provide useful and reliable locations of key features like standard wind radii and RMW from aircraft reconnaissance observations. However, the radial and azimuthal smoothing needed to make wind estimates in unobserved areas affects the analysis of wind extremes. Here,

[4] In 2017 and subsequent years, NHC noticed a discrepancy between SFMR surface wind speed estimates and surface winds estimated from flight-level observations. The differences were most noticeable in TCs with intensities above 115 kt. Investigation with a larger dropwindsonde-based near-surface winds database shows high biases of 1, 5, 7, and 10 kt at 80 kt, 120, 140, and 165 kt in SFMR surface winds estimates, respectively (H. Holbach 2021, personal communication).

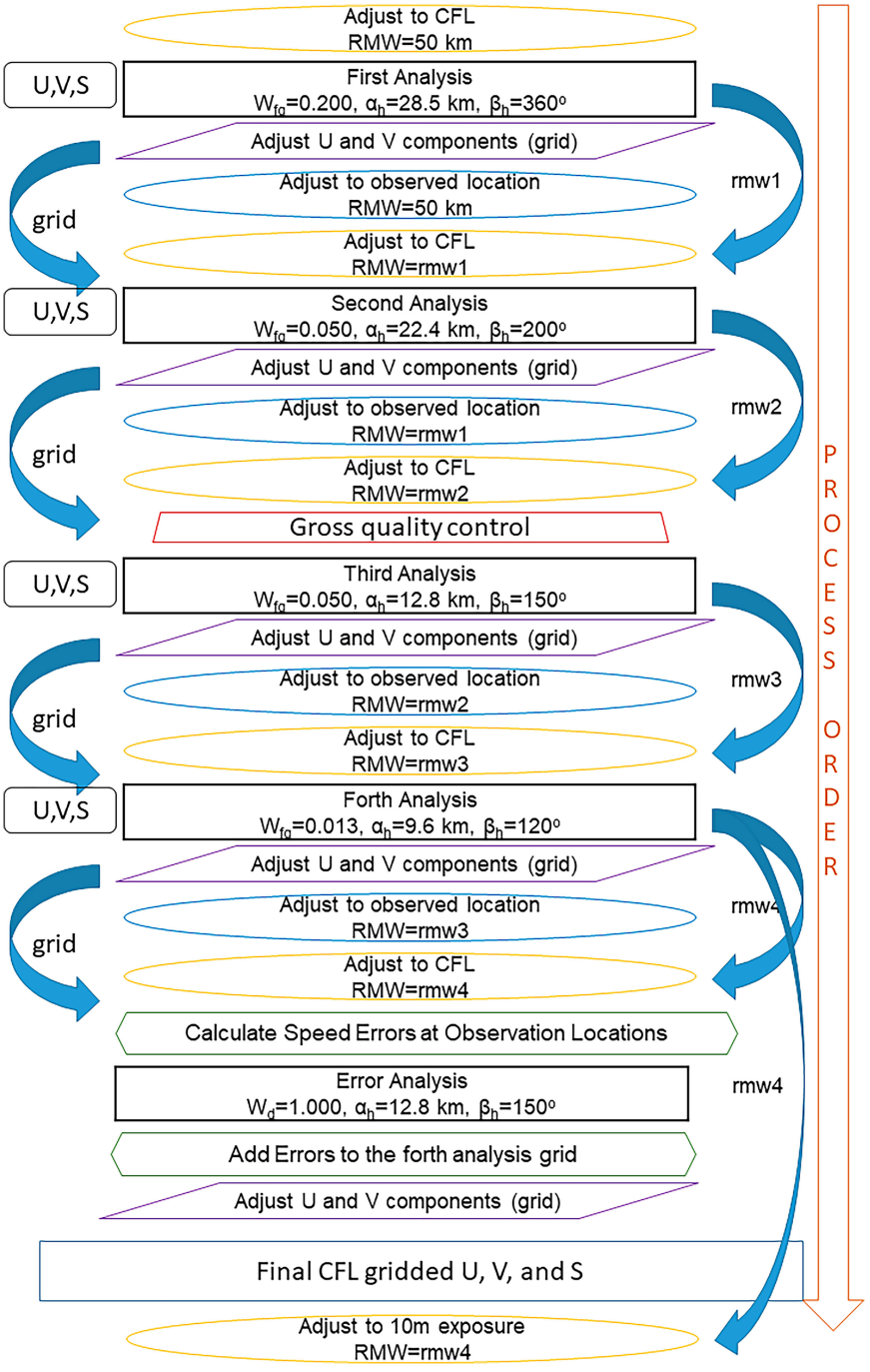

FIG. 3. A schematic of the objective analysis process outlining the changes to data weights w and half powers, α and β, that correspond to each step. Here U, V, and S are the zonal and meridional components of the wind and wind speed, respectively.

we examine the final analysis versus input wind speeds at the CFL, i.e., prior to adjusting those analyses to the surface, to explore how closely the analysis represents the input observations. This comparison avoids the complication of the spatially dependent flight-level to surface wind speed reduction factors. In the case of SFMR, the surface wind speed observations are adjusted (increased) using the same reduction factors used to adjust flight-level winds to surface observations in the final analysis.

We first present the comparison of CFL SFMR OBITUS analysis versus SFMR observations adjusted to the CFL as a function of wind speed (Fig. 4a). This comparison provides the reliability of wind speed ranges based on SFMR observations.

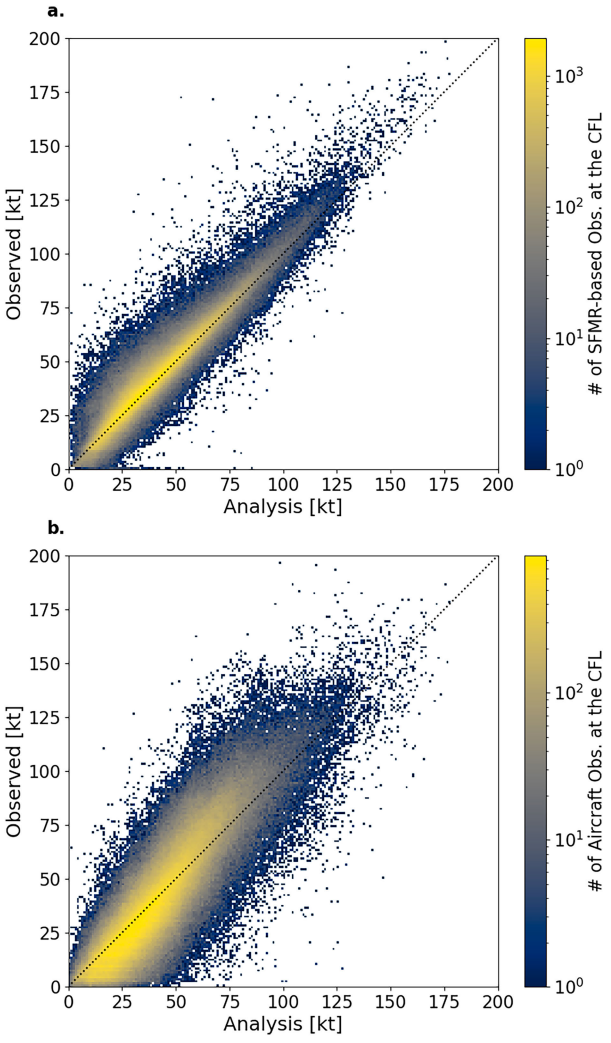

FIG. 4. OBITUS analyses binned by observed wind speeds vs the corresponding average of observed points. This provides a visual estimate of the reliability of wind speed analysis at flight level for (a) SFMR surface wind speeds adjusted to the CFL (700 hPa) from the surface and (b) flight-level wind speeds. The black dotted line represents a perfect match between the analysis and the observations. Please note the ranges in the logarithmic scale of (a) and (b) are different with a smaller number of observations in bins in (b), indicating greater scatter.

Here, we interpolate analysis values to the observation locations. The comparison is based on 743 316 observations collected from 2010 to 2022 and the observations are binned by observed values every 1 kt. In a perfect analysis, the binned observations would correspond 1:1 with the binned analysis. The analyses show low biases by points above and high biases below the 1:1 line. SFMR wind speed analyses are slightly low-biased overall, with small biases below 90 kt and larger underestimations above 100-kt wind speeds. Below ~65 kt, the scatter is somewhat larger. These results are expected given that the analysis will smooth steep wind gradients, and the weaker weighting of SFMR below 75 kt, but the bias increasing linearly and becoming pronounced at the highest wind speeds is unexpected. We feel this result may result from spatial mismatches between flight-level winds and/or surface SFMR caused by sloping eyewalls and center locations, and radial smoothing of steep gradients.

Figure 4b shows a similar OBITUS analysis for 831 388 30-s aircraft-based wind speed observations adjusted to the CFL. Note the color bar ranges for Figs. 4a and 4b are different to better display the ranges contained in the bins and the observational distributions. The aircraft-based winds have more scatter than SFMR observations with an indication of slight high biases at the lowest wind speeds and more pronounced low biases above 65 kt.

The combination of Figs. 4a and 4b suggests that the OBITUS analysis systematically underestimates the wind speed at the CFL. The SFMR-based OBITUS analysis underestimates SFMR observations at all wind speeds whereas the aircraft-based OBITUS analysis underestimates aircraft observations above ~65-kt wind speeds and overestimates aircraft observations below ~50-kt wind speeds. However, this is only part of the story. We next examine the analysis error distributions as a function of radius.

Figure 5a shows the density of biases of the CFL SFMR OBITUS analysis as a function of radius. The wind speed biases at each radial 2 km × 1 kt bin are not as variable as one may suspect. The binned observations show that the majority of the analyzed SFMR wind speeds agree well with the SFMR observations. In addition, the agreement between analyzed SFMR wind speeds and SFMR observations appears at all radii, but with a very slight tendency to be low biased. The largest scatter and most pronounced biases occur around 25 km. The larger biases near the center are consistent with too much smoothing, effects caused by small errors in the center location, and mismatches due to the sloping radius of maximum wind. Figure 5b shows the biases of the aircraft-based OBITUS wind speed analysis in the same way as in Fig. 5a. Note again the color bar has a smaller range in Fig. 5b; indicating greater scatter. Here these figures indicate that the tendency for OBITUS analyses to underestimate the aircraft-based wind speeds with the largest underestimate occurring inside ~40 km. The analyses' inner core flight-level wind low biases mirror the high biases in analyzing the SFMR suggesting the analysis lies between overestimated SFMR winds and underestimated aircraft wind speeds. Elsewhere, these biases mirror each other to a lesser degree, but the analyses agree much better with the SFMR observations.

To provide readers a better idea of the fit to observations in individual cases with differing intensities, data coverages, and wind structure, difficult to infer from Figs. 4 and 5, the supplemental material provides three additional cases from the 2018 North Atlantic hurricane season, Major Hurricane Michael, Hurricane Florence, and Tropical Storm Alberto that more closely examines three individual cases.

b. *Examination of analysis sensitivity to observational coverage*

In this section, we use a method similar to Uhlhorn and Nolan (2012) to construct 700-hPa wind vectors and SFMR

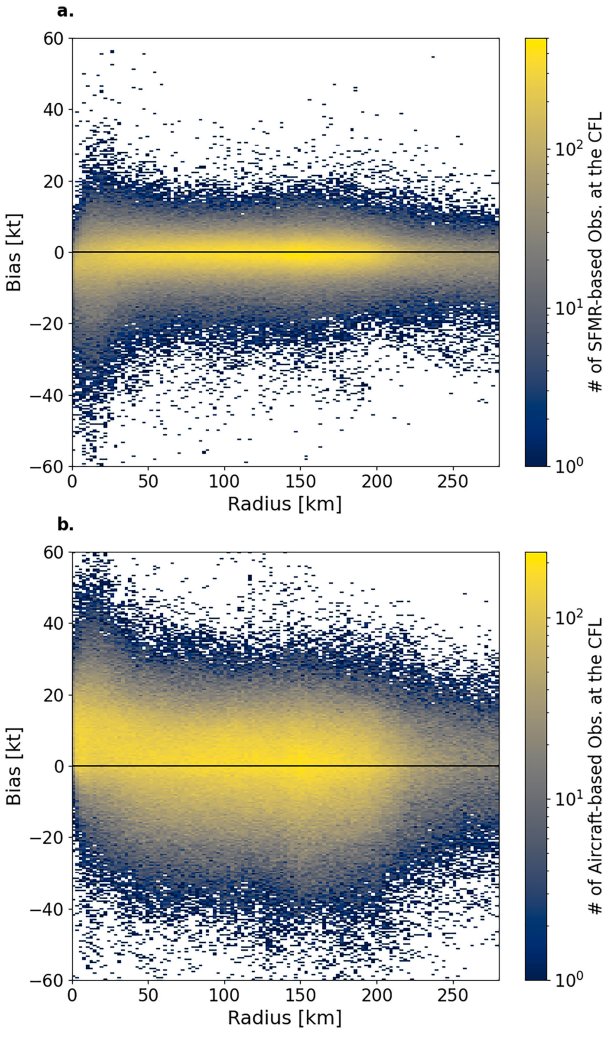

FIG. 5. Distribution of analysis errors (kt) for the OBITUS analysis of (a) SFMR-based wind speeds and (b) aircraft-based wind speeds, both at the CFL, as a function of radius. The grid is binned 2 km × 1 kt, and the color bar to the right of each panel provides the logarithm of counts. Please note the ranges in the logarithmic scale of (a) and (b) are different with smaller number of observations in bins in (b), indicating greater scatter.

(10-m) wind speed directly from the operational forecasts of the Hurricane Weather Research and Forecast (HWRF) Model to test the sensitivity to observational coverage (and not a comprehensive assessment of skill). In this sensitivity analysis, we assume that HWRF has a similar relationship between 700-hPa winds and the 10-m winds provided in nature, and that HWRF wind-averaging periods are the same as the HDOBS. We pick three flight patterns from those observed: enhanced coverage, an alpha pattern, and a single transect across the entire storm. Unlike Uhlhorn and Nolan's work, we want to determine how well the analysis system can reconstruct the "observed" 2D surface wind field (10-m HWRF winds) with the limited observations of the simulated flight patterns and assess how the observational coverage affects the resulting analysis's ability to capture key features in the 2D wind field. For these analyses, we used the same first guess used for real-time analyses.

Because HWRF structural features are larger than those typically observed in nature, especially in the inner core (e.g., Dong et al. 2020), we halved the radial distances before creating the simulated flight-level and SFMR observations. This should provide a more realistic inner core size and radius of maximum wind for investigating the sensitivity to observational coverage. The scaling also ensures that the synthetic aircraft observations extend beyond the 34-kt winds in most quadrants. We use three separate initialization times and 6-h forecasts from Hurricane Teddy (2020) as our cases, valid 0000 UTC 18 September (Case 1), 1200 UTC 20 September (Case 2), and 1800 UTC 20 September (Case 3). From these scaled model outputs, the enhanced, alpha pattern, and single transect inputs are created. Root-mean-square error (RMSE) for the entire field, intensity and wind radii statistics are provided for our three cases. Note the supplemental material provides analysis sensitivity results based on the non-scaled synthetic observations. The three differing flight-level patterns show that improved observational coverage produces 2D analyses with smaller errors (Table 3 and Table S2 in the online supplemental material). All analyses underestimate the maximum winds, provide good estimates of RMW, and have slightly smaller 34- and 50-kt wind radii (Table 3). The limited sampling likely causes the latter.

Summary statistics (Table 3), however, provide scant details of how the wind fields are spatially different. To provide readers with these details, we examine the details of Case 3. Case 3 is a weakening hurricane with a large asymmetric RMW; here, the analysis uses a first guess from the satellite-only analysis valid 1500 UTC 20 September. At 1800 UTC 20 September, the vortex tracker (Marchok 2002, 2021) indicated that HWRF had a 74-kt intensity and a 51 n mi RMW, corresponding to 26 n mi in our scaled inputs.

Figure 6 shows the Case 3 analyses (Figs. 6a,e,i), the observed winds with flight paths (Figs. 6b,f,j), the spatial biases (Figs. 6c,g,k) and the scatterplot of the winds with color coated biases (Figs. 6d,h,l) for the three flight patterns. The supplemental material provides similar figures for Cases 1 and 2 (Figs. S5 and S6) and for analyses based on non-scaled inputs for Cases 1, 2, and 3 (Figs. S7–S9). The enhanced observational coverage, Fig. 6a, results in a 73-kt max intensity and a 28 n mi RMW. However, the details of the observed vortex (Figs. 6b,f,j) are quite interesting with a rather asymmetric region of wind exceeding 64 kt, and 34-kt winds protruding to the east of the center. All the analyses are more symmetric than the observed wind field due to the azimuthal smoothing. The azimuthal smoothing and the lack of flight level observations in the eastern regions (Figs. 6c,g,k) remove the observed bulge of 34-kt winds to the east, and the southernmost extension of 64-kt winds to the southeast. Those negative biases (Fig. 6c) exist even in the enhanced observation analysis (Fig. 6a). Similarly, the effects of the radial smoothing in the southern and south-southeast portion of the TC's core results in a pronounced high wind speed anomaly that increases with reduced observational coverage (Figs. 6c,g,k). Bias plots also

TABLE 3. Statistics for our three cases from both the scaled HWRF surface wind fields and intensity, RMW, and wind radii estimates via the vortex tracker (Marchok 2002, 2021). The surface wind analyses used enhanced, alpha pattern, and single transect observational coverage as described in the text. Shown are the RMSE of the entire wind field (kt) along with analysis estimates of intensity (kt), RMW (n mi), and 34-, 50-, and 64-kt wind radii, denoted as R34, R50, and R64, respectively. R34, R50, and R64 values are listed for northeast, southeast, southwest, and northwest quadrants (shown from left to right), and have been rounded to the nearest 5 n mi increment. RMW and wind radii from the observations are half those provided by the operational HWRF tracker as the wind field is radially scaled by 0.5, and rounded to the nearest nautical mile.

	Observed				Enhanced				Alpha				Single			
Case 1 (valid at 0000 UTC 18 Sep)																
RMSE					2.52				4.82				7.12			
Intensity		111			101				102				98			
RMW		19			18				17				18			
R34	89	85	57	89	80	75	60	80	90	90	80	85	80	80	80	120
R50	63	45	33	55	55	45	35	45	55	55	45	55	45	40	45	45
R64	35	29	29	37	30	25	30	35	40	40	30	35	35	30	35	35
Case 2 (valid at 1200 UTC 20 Sep)																
RMSE					2.24				3.88				5.47			
Intensity		82			78				75				73			
RMW		30			31				30				26			
R34	106	104	77	88	90	90	80	85	90	90	80	85	100	100	90	95
R50	64	64	50	50	55	55	45	55	55	55	50	55	55	55	55	50
R64	49	44	36	36	40	40	30	35	45	40	30	40	30	30	30	30
Case 3 (valid at 1800 UTC 20 Sept)																
RMSE					2.64				3.46				4.26			
Intensity		74			73				71				72			
RMW		26			28				26				25			
R34	106	108	77	77	85	85	80	75	85	85	80	75	80	90	90	80
R50	60	61	49	48	55	55	40	50	55	50	45	50	45	50	50	45
R64	39	40	32	39	35	30	30	35	35	30	30	35	35	30	35	35

show the impact of the first guess that had stronger winds than observed in the outer regions of the storm, where beyond the observational coverage high biases emerge (Figs. 6g,k). The inner core becomes more symmetric as observational coverage decreases. Again, the difference shows a sensitivity to the first guess outside observational coverage and to impacts caused by the azimuthal and radial smoothing (south of the core), in regions where there are no aircraft-based nor SFMR-based observations. In the single transect case, the inner core asymmetries reverse, which is indicated by the associated biases (Fig. 6k). The scatterplots show that the scatter increases with reduced observational coverage, but both the enhanced and alpha cases have very few points where the biases exceed ±10 kt. The biases in the single transect case are exacerbated by the flight path being aligned with storm motion (~325°), where motion-induced wind asymmetries would be minimal. Case 3 with its pronounced asymmetries, demonstrates how the observational coverage, imperfect first guess, and different azimuthal and radial smoothing effects the analyzed surface wind field.

c. *Examples compared with SAR*

While independent, in situ TC surface wind observations are unavailable for verification, promising satellite-based wind speed observations can provide some independent verification. The C-band SAR available on *RadarSat-2*, *Sentinel-1A*, and *Sentinel-1B* have a cross-polarized mode that allows for high spatial resolution, and nearly instantaneous retrievals of extreme wind speeds found in TCs [detailed discussions in Mouche et al. (2017, 2019) and Knaff et al. (2021)]. While overpasses of TC scenes are becoming more common, overpasses are infrequent due to operational procedures and constraints. Here we have selected three recent cases to compare with the surface wind analysis. The data availability statement describes the observations.

We provide a visual comparison of the wind speeds from both SAR and the analysis at native resolutions with error estimates at a reprocessed resolution. With SAR wind products being available at 500-m spatial resolution and able to resolve higher wind speeds; a two-pass Barnes (1964) analysis is performed with an *e*-folding radius of 12 km to provide a reasonable comparison to the resolving capabilities of the surface wind analysis. We remind readers that SAR winds are nearly instantaneous and our analysis composites observations over the most recent 8 h. Table 4 provides details of the SAR cases used for comparisons.

The first example is from Hurricane Michael (2018; Beven et al. 2019) at 1200 UTC 10 October, also see the supplemental (Figs. S1 and S4a). Figure 7 shows (Fig. 7a) the surface wind analysis, (Fig. 7b) 500-m resolution SAR wind speed product from *Sentinel-1A*, and (Fig. 7c) flight level wind barbs, respectively. The analysis resolves a realistic RMW and reasonable estimates of the 34- and 64-kt wind radii as indicated by discontinuities in the color scale. SAR captures higher wind speeds on the north to east portion of the eyewall—the two closely spaced maxima near the center just outside the RMW are likely due to high rain rates in the eyewall (Mouche

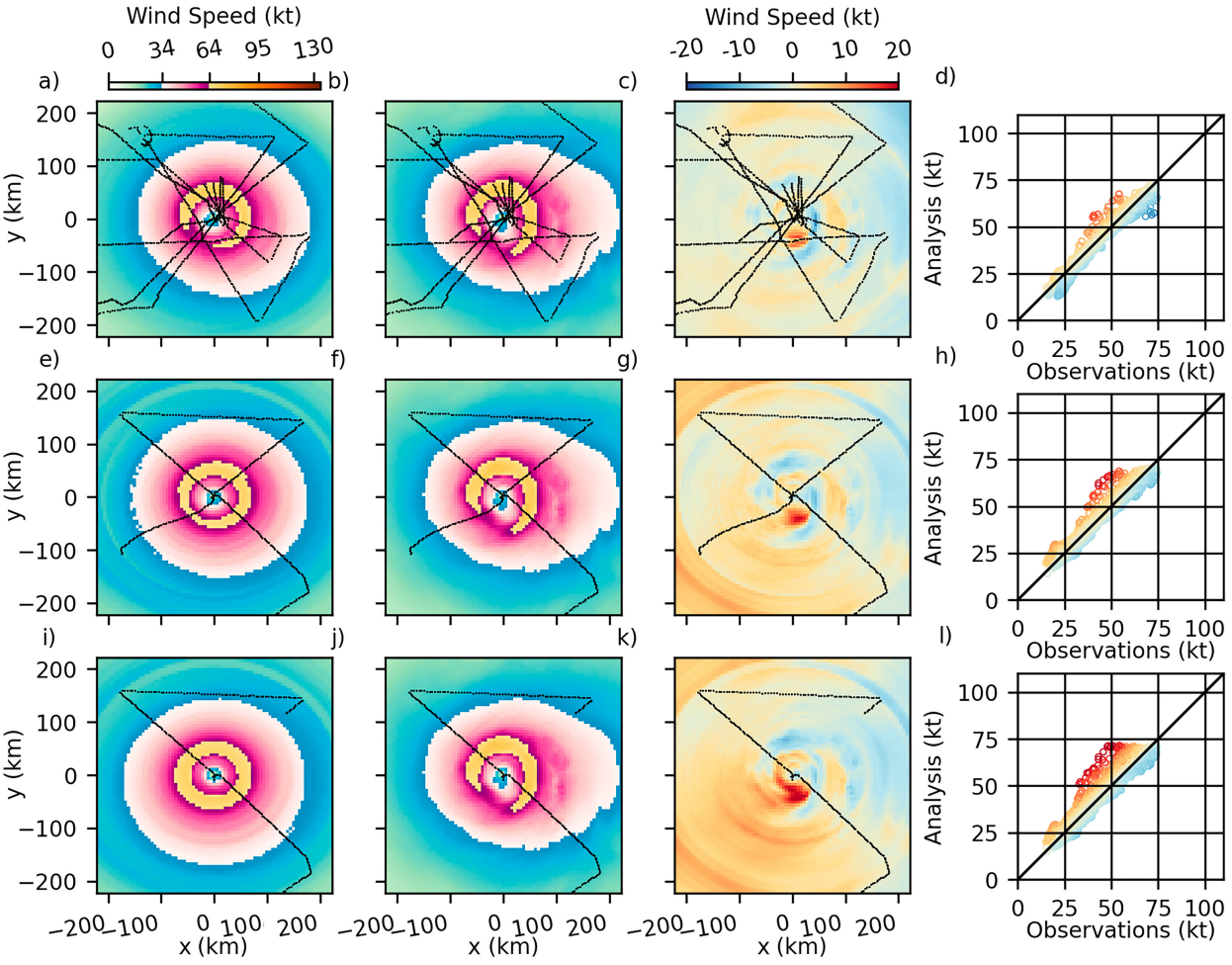

FIG. 6. Results based on the 6-h forecast HWRF 10-m winds valid at 1800 UTC 20 Sep 2020 for Hurricane Teddy (Case 3) where the radial distances have been scaled by a factor of 0.5. Analysis results for (a) enhanced, (e) alpha pattern, and (i) single transect observational coverage; (b),(f),(j) observed 10-m winds; (c),(g),(k) analysis biases; and (d),(h),(l) observations vs analysis scatterplots. The observational coverage on all panels except the scatterplots provide the tracks of the synthetic aircraft tracks (black lines). The magnitude of the wind speeds is provided on the analyses and observations panels, and biases are shown in both the bias panels and the scatterplots as indicated by the colors in the color bars located above (a) and (c), respectively.

et al. 2019), and not indicative of a secondary eyewall. Note that a secondary eyewall/wind maximum is not evident in the aircraft reconnaissance observations (Figs. S1 and S4c) nor in radar (Cha et al. 2020). SAR also shows stronger winds on the northwestern and southwestern sides where the radial decay in wind speeds is largest. Both SAR and the analysis show the lopsided nature of the winds in Michael with winds exceeding 64 kt extending southeast of the center. In the inner core region, the analysis shows lower wind speeds than the SAR. In outer regions, the maximum extent of 34-kt winds between the analysis and SAR are comparable except in the northwestern region of the storm. The scatterplot in Fig. 7d compares the resolution-corrected SAR and the analysis calculated within 90 n mi (166 km) from the storm center, and shows underestimates of winds in the core and overestimates below wind speeds of approximately 40 kt. It is noteworthy that during the ~8-h time of observation collection, Michael was intensifying with a 5-kt increase and 11-hPa decrease in

TABLE 4. Details of the comparisons between the surface wind analysis and SAR-based winds speeds from *Sentinel-1A/B* and *RadarSat-2*. Intensities of 2018 and 2020 final best tracks.

Storm	Analysis time and date	SAR time	Satellite	Intensity
Hurricane Michael	1200 UTC 10 Oct 2018	1150 UTC	*Sentinel-1A*	125 kt
Hurricane Delta	0000 UTC 8 Oct 2020	0008 UTC	*Sentinel-1B*	80 kt
Hurricane Laura	1200 UTC 25 Aug 2020	1135 UTC	*RadarSat-2*	65 kt

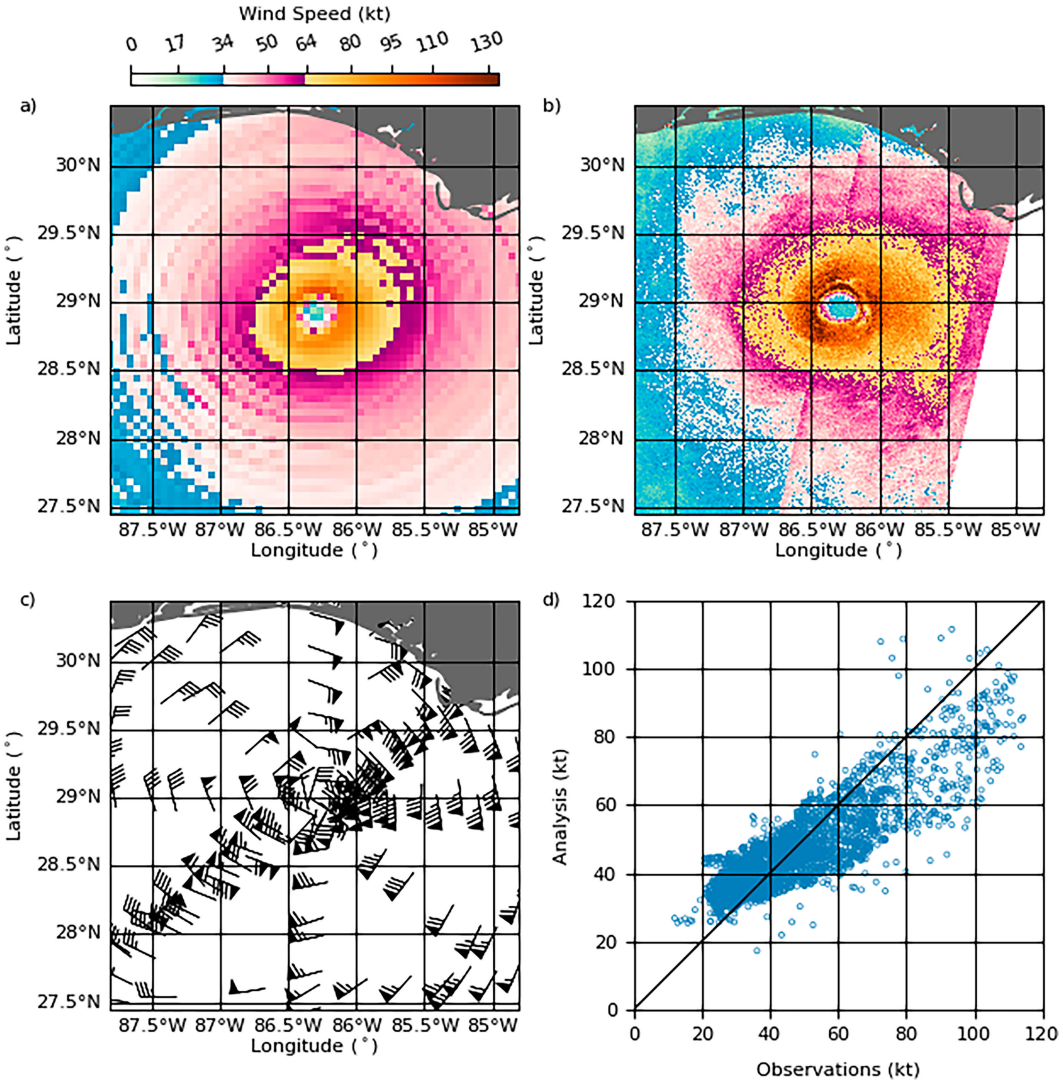

FIG. 7. (a) Surface wind analysis for Hurricane Michael (2018) valid at 1200 UTC 10 Oct, (b) wind retrieval from the 1150 UTC 10 Oct *Sentinel-1A* SAR overpass, (c) thinned flight-level aircraft reconnaissance observations, and (d) a scatterplot showing how the SAR winds from the two-pass Barnes analysis compare to those in the final analysis. Gray regions in (a)–(c) indicate landmasses.

the final best track between 0600 and 1200 UTC (Beven et al. 2019). These changes in the storm intensity likely led to some biases, but there is still reasonable agreement between SAR and analyzed wind speeds with a root-mean-square deviation of 10.5 kt calculated within radii of 90 n mi of the center. The analysis produced wind radii features that agreed with both the SAR and the NHC best track. The analysis estimated the RMW to be 11 n mi versus 9 n mi in the SAR. The analysis found a maximum wind of 113 kt versus 135 kt from SAR and 125 kt from NHC's best track. The azimuthally averaged 34-, 50-, and 64-kt wind radii also agreed well among all three sources, except the SAR had a larger averaged 64-kt wind radius (53 n mi versus ~33 n mi).

The second case, Hurricane Delta (2020), a nonmajor hurricane, started to intensify after passing over the Yucatán Peninsula reaching 80 kt by 0000 UTC 8 October, and was intensifying, 5 kt, −5 hPa during the observation compositing (Cangialosi and Berg 2021). The SAR estimated a maximum wind of ~78 kt with a RMW of 22 n mi, whereas the analysis estimated 67 kt and 20 n mi, respectively. Based on Figs. 8a and 8b, the region with 34-kt or stronger winds is much larger in the surface analysis, but seems partially supported by the 700-hPa observations. The analysis does a good job in this case of providing inner core estimates of winds and indicating narrow and near circular wind maximums. The RMW is similar between the analysis and SAR, but in-eye wind speeds are quite a bit higher in the SAR, which is evidence of the analysis' smoothing. The secondary wind maximum north of the storm in SAR, is also absent in the analysis and in the aircraft observations (Fig. 8c). Given the analysis' azimuthal smoothing and the nearly instantaneous SAR observations are nearly 34 kt, slight differences are not surprising. Scatterplots in Fig. 8d

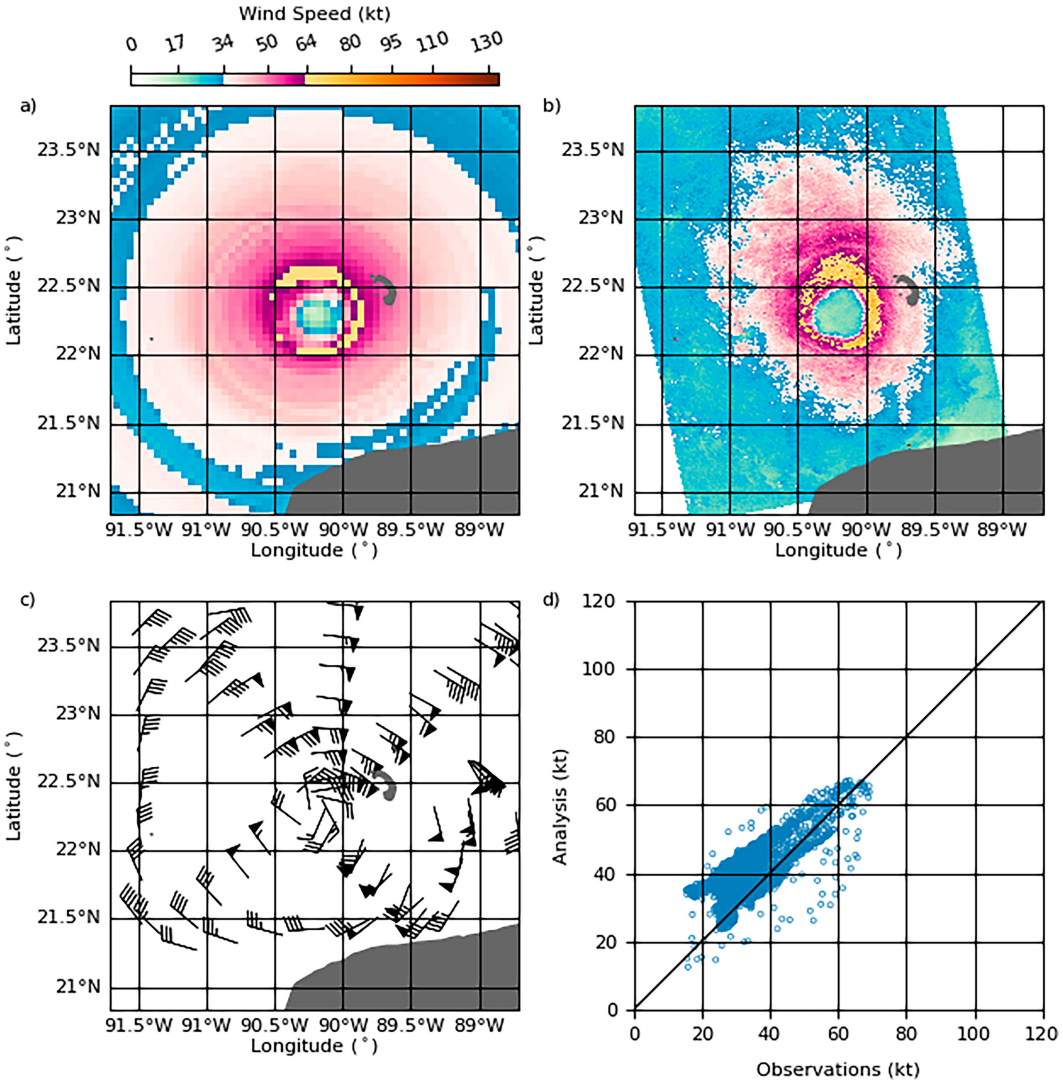

FIG. 8. As in Fig. 7, but for Hurricane Delta (2020) valid at 0000 UTC 8 Oct with the coincident wind retrieval from the 0008 UTC 8 Oct *Sentinel-1B* SAR overpass.

show details of the differences, where a slight high bias appears in the surface analysis. For this case, the root-mean-square deviation calculated within 90 n mi is 8.6 kt.

The third case is from Hurricane Laura (2020) after moving from the Sierra de los Órganos in western Cuba to the Gulf of Mexico. At 1200 UTC 25 August, Laura started regaining strength, intensifying by 5 kt in the past 6 h, and had estimated maximum winds of 65 kt (Pasch et al. 2021). The analysis estimated the maximum winds at 61 kt with a RMW of 44 n mi versus 65 kt and 32 n mi, respectively, from SAR. The wind structure was highly asymmetric as shown in both the analysis and *RadarSat-2* SAR wind speeds in Figs. 9a and 9b. In both wind speed estimates, the asymmetrical region of 50-kt winds is located 100 km to the north and east of the circulation center. However, in this case, SAR misses the pocket of 50-kt winds on the northern side of Laura's eyewall evident in the aircraft flight-level observations (Fig. 9c). In general, the analysis is more symmetric than the SAR retrievals due to the azimuthal smoothing. From the scatterplot in Fig. 9d, the analysis shows this high bias in winds less than 40 kt predominantly in the northeast and southwest storm quadrants (see Fig. 9c). The root-mean-square deviation calculated within 90 n mi is 16.6 kt.

TC interaction with land affects the surface wind field and results in weaker winds than will be observed over the open ocean. In the Delta and Laura cases, the TCs had moved off land implying that the winds in the boundary layer will be weaker than the winds observed at flight level. This is evident in Laura where the strongest SAR winds are collocated with convection (not shown) and allows midlevel winds to mix down to the boundary layer. The analysis does not factor in the time since land interaction, which likely accounts for much of the analyses' high biases in the Delta and Laura cases.

Overall, the aircraft-based analysis captures the wind fields shown in the SAR wind speed retrievals. We reiterate that

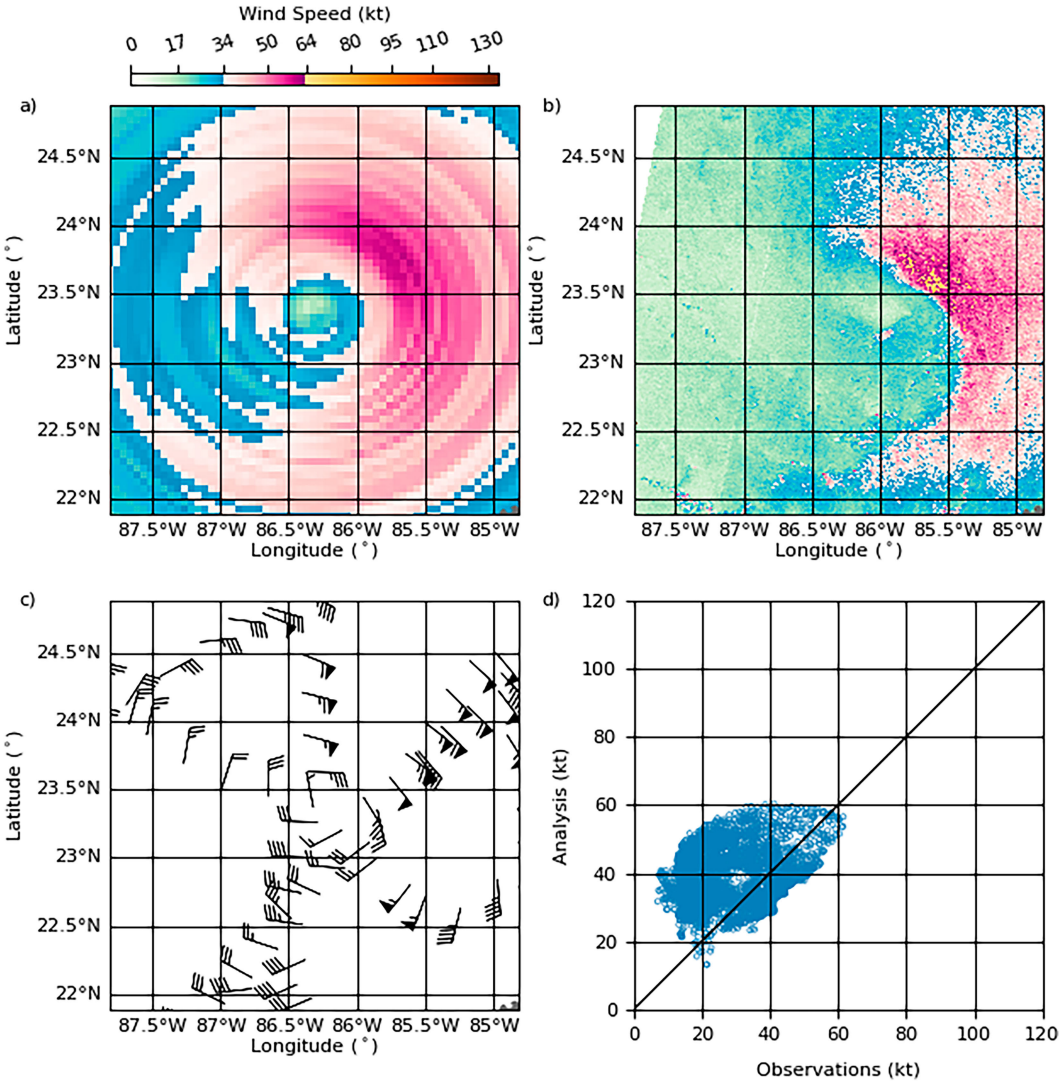

FIG. 9. As in Fig. 7, but for Hurricane Laura (2020) valid at 1200 UTC 25 Aug with the coincident wind retrieval from the 1135 UTC 25 Aug *RadarSat-2* SAR overpass.

SAR wind speeds are nearly instantaneous and that the retrievals are indirect estimates of the wind speed. Given that background, the shortcomings of the analyses seem to be related to compositing several hours of observations, not capturing boundary layer changes (Laura and Delta), and the necessity of radial and azimuthal smoothing. It is also not surprising that underestimation of the maximum wind is systematic in the analyses due to aircraft under sampling. Uhlhorn and Nolan (2012) found average underestimates of peak wind of about 8.5%, and Klotz and Nolan (2019) found underestimates ranging from 0% to 17% depending on eye size and sampling strategy.

5. Summary and discussion

This paper documents a real-time surface wind analysis for TCs observed by low-level aircraft reconnaissance. The analysis uses both flight-level wind vectors and surface SFMR-based wind speed estimates combined in a storm-following manner in time windows ≤ 8 h. The winds are adjusted to a common 700-hPa analysis level or CFL using a set of flexible and changeable flight-level to surface reduction factors. The analysis is performed on a polar grid and uses an iterative approach with variable observation type-based weights and smoothing constraints. Real-time HDOBS provide flight-level and SFMR wind information every 30 s, and ATCF working best tracks, aircraft center fixes, and official forecasts provide center-tracking information. To extend the information contained in aircraft observed transects, separate azimuthal and radial smoothing constraints are applied. The analysis is run several times progressively decreasing the radial and azimuthal smoothing constraints and readjusting the observed winds to the CFL using updated RMW estimates, the OBITUS analysis. By progressively reducing the smoothing, the analysis captures the information in the observations including the RMW, which

is critical to adjusting the final analysis to the 10-m surface, and assigning inflow angles. Finally, if the points are overland the winds are reduced by another 20% and the inflow is increased by an additional 20°.

The aircraft flight-level observations are under analyzed while the SFMR winds at the CFL are better estimated as a function of radius. These underestimates are likely due to the use of azimuthal and radial filters, data weights, and under sampling maxima and minima in the wind observations. The resulting analyses, however, capture the bulk vortex characteristics. Using synthetic model-based observations, we show that as the observational coverage increases, the errors and biases become smaller, and reveal a sensitivity to the first guess, in regions where there are no aircraft-based nor SFMR-based observations. Finally, through demonstrations based on observed SAR surface wind retrievals and synthetic flight-level and SFMR transects, the resulting analysis produces a realistic, yet more symmetric, wind field based on few in situ observations.

We recognize that this is a simple analysis system in comparison to advanced data assimilation methods, and with additional funding and effort, further improvements are possible. This method does have the advantage that it is observation driven and provides a useful analysis of the inputs, relies on simple polar geometry, is available in a timely manner, and exists today. We see two advantages over advanced data assimilation, model errors caused by grid geometry, resolution, boundary layer assumptions and microphysics do not affect the final analysis, and the analysis provides surface wind analyses that are not reliant on the data assimilation system spreading information efficiently. This analysis provides a baseline for analyses produced by more advanced methods. The analysis method described here has different shortcomings. It produces symmetric analyses due to the necessary smoothing of limited observations in the azimuthal and radial directions, and it struggles when the observed storm structure and/or intensity evolve quickly during the 8-h analysis window.

It is also worth noting that we have used a large compositing window to create input observations. We use this strategy to create as many analyses as possible given the relative rarity of these observations. It is also noteworthy that in most cases, the reconnaissance target times are close to the synoptic hours of 0000, 0600, 1200, and 1800 UTC, so the 8-h period often contains one sortie and one centered on the analysis time. However, TCs do evolve over any period, and an 8-h window can include some dramatic changes in intensity and structure. We examined the variability that can occur during an 8-h compositing time by comparing the 8-h mean with values at the aircraft fix times. We specifically examined intensity, the nonzero averaged 34-kt wind radii, and RMW values 2004–22. Interpolated estimates of intensity and 34-kt winds come from the final best track estimates whereas RMW estimates come directly from the aircraft estimates. Both the best tracks and the fix information come from the ATCF databases. The results of this analysis suggest that 96% of the intensity differences are between ±10 kt and 85% of the fixes azimuthally averaged 34-kt wind radii are within ±10 n mi. On the other hand, the RMW can show quite a bit of variability with only 70% of the RMW fixes being within ±20 n mi of the 8-h mean value. The distribution of the percent differences from the 8-h mean RMW in this analysis shows the quartiles of the distribution ranging roughly 20%–35%. In addition, RMW values are skewed toward larger values. It is noteworthy that fixes of RMW are noisy by the nature of the estimates, i.e., as the maximum along both inbound and outbound legs. This simple analysis suggests that in most cases intensity and structure are within typical uncertainties of intensity estimation (Torn and Snyder 2012; Landsea and Franklin 2013) and 34-kt wind radii (Sampson et al. 2018; Combot et al. 2020). However, RMW estimates are less trustworthy and likely to be larger than observed instantaneously, a result that is similar to the comparison of best track RMW and SAR-based estimates (Fig. 9, Combot et al. 2020). Finally, this is a data-fitting method, so regions outside the radius of maximum observational coverage could be erroneous as they become reliant on the first guess.

It is also important to realize that as SFMR algorithms change and guidance on how to estimate surface winds from the flight/analysis level evolve, the algorithm can adjust to those new inputs and can reflect new flight-level to surface reduction methodologies. In the future, we want to conduct more comparisons with SAR, and to compare the output of these analyses to the ideas and concepts presented in Uhlhorn et al. (2014). There are also new data platforms becoming available that may provide additional sources of observations and validation to better estimate the surface winds in tropical cyclones (Holbach et al. 2023). Also, this analysis could make use of tail Doppler winds (e.g., Rogers et al. 2012) processed in real time aboard the NOAA reconnaissance aircraft, and will be explored soon.

These analyses can likely be improved with additional efforts. These include accounting for the slope of the radius of maximum winds between flight-level and surface observations, the application of a more realistic boundary layer scheme as the vertical column assumption used to reduce the analysis to the 10-m surface is also a known shortcoming (e.g., Kepert 2001), and the addition of other observations, when available. In this work, we have identified the sensitivities to the first guess, and future work will target this shortcoming, using the global models that have shown the ability to estimate the maximum extent of 34-kt winds with useful accuracy (Knaff and Sampson 2015; Sampson and Knaff 2015; Sampson et al. 2017, 2018).

This manuscript provides the documentation for these analyses that have proved useful for several applications. Analyses have been generated in real time since the 2010 hurricane season though the algorithm was only recently finalized. Analyses have many applications beyond providing real-time assessments. Past analyses have been rerun using the final algorithm and are freely available as described in the data availability statement. Finally, through work with NHC, the analyses are now produced in their local computational environment (since 2021), and analysis fixes are available in the operational ATCF fix database.

Acknowledgments. This work was supported through the authors' employment with the NOAA Center for Satellite Applications and Research in support of a number of tropical

cyclone applications. We acknowledge the previous three anonymous reviewers who provided constructive comments on this work that led to a much-improved manuscript. The NOAA Joint Hurricane Testbed provided funding for the development of this application (NA17RJ1228), and we thank Alan Brammer, the Hurricane and Ocean Testbed Facilitator, for getting the algorithm running at NHC. We also thank all those that collected, disseminated, and archived the aircraft reconnaissance observations and SAR wind speed observations used here. The scientific results and conclusions, as well as any views or opinions expressed herein, are those of the author(s) and do not necessarily reflect those of NOAA or the Department of Commerce.

Data availability statement. This publication uses real-time aircraft reconnaissance, tropical cyclone forecasts, and fixes, which are openly available from the National Hurricane Center. Resulting analyses are available from CIRA and NESDIS. The following provides observation types followed by locations where data availability can either be directly accessed or registration for access can be initiated: 1) HDOBS from https://www.nhc.noaa.gov/recon.php, 2) TC forecasts and fixes from ftp://ftp.nhc.noaa.gov/atcf/, 3) past and real-time analyses ftp://rammftp.cira.colostate.edu/knaff/JHT-TCSWA/, and 4) SAR tropical cyclone wind from NOAA Center for Satellite Applications and Research SAR Products page https://www.star.nesdis.noaa.gov/socd/mecb/sar/AKDEMO_products/APL_winds/tropical/tropical_merged_2.html.

REFERENCES

Barnes, S., 1964: A technique for maximizing details in numerical weather map analysis. *J. Appl. Meteor.*, **3**, 396–409, https://doi.org/10.1175/1520-0450(1964)003<0396:ATFMDI>2.0.CO;2.

Beven, J. L., II, R. Berg, and A. Hagen, 2019: Tropical cyclone report: Hurricane Michael (7–11 October 2018). NHC Tech. Rep. AL142018, 86 pp., https://www.nhc.noaa.gov/data/tcr/AL142018_Michael.pdf.

Boose, E. R., K. E. Chamberlin, and D. R. Foster, 2001: Landscape and regional impacts of hurricanes in New England. *Ecol. Monogr.*, **71**, 27–48, https://doi.org/10.1890/0012-9615(2001)071[0027:LARIOH]2.0.CO;2.

Brennan, M. J., 2019: NHC's use of aircraft data in hurricane analysis. SECART 2019 Resilience Webinar Series, 22 pp., https://www.noaa.gov/sites/default/files/legacy/document/2020/Dec/SECARTwebinar-Brennan-sm.pdf.

Cangialosi, J. P., and R. Berg, 2021: Tropical cyclone report: Hurricane Delta (4–10 October 2020). NHC Tech. Rep. AL262020, 46 pp., https://www.nhc.noaa.gov/data/tcr/AL262020_Delta.pdf.

Cha, T.-Y., M. M. Bell, W.-C. Lee, and A. J. DesRosiers, 2020: Polygonal eyewall asymmetries during the rapid intensification of Hurricane Michael (2018). *Geophys. Res. Lett.*, **47**, e2020GL087919, https://doi.org/10.1029/2020GL087919.

Cline, I. M., 1920: Relation of changes in storm tides on the coast of the Gulf of Mexico to the center and movement of hurricanes. *Mon. Wea. Rev.*, **48**, 127–146, https://doi.org/10.1175/1520-0493(1920)48<127:ROCIST>2.0.CO;2.

Combot, C., A. Mouche, J. Knaff, Y. Zhao, Y. Zhao, L. Vinour, Y. Quilfen, and B. Chapron, 2020: Extensive high-resolution synthetic aperture radar (SAR) data analysis of tropical cyclones: Comparisons with SFMR flights and best track. *Mon. Wea. Rev.*, **148**, 4545–4563, https://doi.org/10.1175/MWR-D-20-0005.1.

De Boor, C., 1978: *A Practical Guide to Splines*. rev. ed. Springer, 392 pp.

DeMaria, M., and R. W. Jones, 1993: Optimization of a hurricane track forecast model with the adjoint model equations. *Mon. Wea. Rev.*, **121**, 1730–1745, https://doi.org/10.1175/1520-0493(1993)121<1730:OOAHTF>2.0.CO;2.

——, and J. Kaplan, 1999: An updated statistical Hurricane Intensity Prediction Scheme (SHIPS) for the Atlantic and eastern North Pacific basins. *Wea. Forecasting*, **14**, 326–337, https://doi.org/10.1175/1520-0434(1999)014<0326:AUSHIP>2.0.CO;2.

Dong, J., and Coauthors, 2020: The evaluation of real-time Hurricane Analysis and Forecast System (HAFS) Stand-Alone Regional (SAR) model performance for the 2019 Atlantic hurricane season. *Atmosphere*, **11**, 617, https://doi.org/10.3390/atmos11060617.

Franklin, J. L., M. L. Black, and K. Valde, 2003: GPS dropwindsonde wind profiles in hurricanes and their operational implications. *Wea. Forecasting*, **18**, 32–44, https://doi.org/10.1175/1520-0434(2003)018<0032:GDWPIH>2.0.CO;2.

Holbach, H. M., and Coauthors, 2023: Recent advancements in aircraft and in situ observations of tropical cyclones. *Trop. Cyclone Res. Rev.*, **12**, 81–99, https://doi.org/10.1016/j.tcrr.2023.06.001.

Holthuijsen, L. H., M. D. Powell, and J. D. Pietrzak, 2012: Wind and waves in extreme hurricanes. *J. Geophys. Res.*, **117**, C09003, https://doi.org/10.1029/2012JC007983.

Kepert, J. D., 2001: The dynamics of boundary layer jets within the tropical cyclone core. Part I: Linear theory. *J. Atmos. Sci.*, **58**, 2469–2484, https://doi.org/10.1175/1520-0469(2001)058<2469:TDOBLJ>2.0.CO;2.

——, 2023: A parametric model of tropical cyclone surface winds for sea and land. *Wea. Forecasting*, **38**, 1739–1757, https://doi.org/10.1175/WAF-D-23-0028.1.

——, and Y. Wang, 2001: The dynamics of boundary layer jets within the tropical cyclone core. Part II: Nonlinear enhancement. *J. Atmos. Sci.*, **58**, 2485–2501, https://doi.org/10.1175/1520-0469(2001)058<2485:TDOBLJ>2.0.CO;2.

Klotz, B. W., and E. W. Uhlhorn, 2014: Improved stepped frequency microwave radiometer tropical cyclone surface winds in heavy precipitation. *J. Atmos. Oceanic Technol.*, **31**, 2392–2408, https://doi.org/10.1175/JTECH-D-14-00028.1.

——, and H. Jiang, 2017: Examination of surface wind asymmetries in tropical cyclones. Part I: General structure and wind shear impacts. *Mon. Wea. Rev.*, **145**, 3989–4009, https://doi.org/10.1175/MWR-D-17-0019.1.

——, and D. S. Nolan, 2019: SFMR surface wind undersampling over the tropical cyclone life cycle. *Mon. Wea. Rev.*, **147**, 247–268, https://doi.org/10.1175/MWR-D-18-0296.1.

Knaff, J. A., and C. R. Sampson, 2015: After a decade are Atlantic tropical cyclone gale force wind radii forecasts now skillful? *Wea. Forecasting*, **30**, 702–709, https://doi.org/10.1175/WAF-D-14-00149.1.

——, M. DeMaria, D. A. Molenar, C. R. Sampson, and M. G. Seybold, 2011: An automated, objective, multiple-satellite platform tropical cyclone surface wind analysis. *J. Appl. Meteor. Climatol.*, **50**, 2149–2166, https://doi.org/10.1175/2011JAMC2673.1.

——, S. P. Longmore, R. T. DeMaria, and D. A. Molenar, 2015: Improved tropical-cyclone flight-level wind estimates using routine infrared satellite reconnaissance. *J. Appl. Meteor. Climatol.*, **54**, 463–478, https://doi.org/10.1175/JAMC-D-14-0112.1.

——, and Coauthors, 2021: Estimating tropical cyclone surface winds: Current status, emerging technologies, historical evolution, and a look to the future. *Trop. Cyclone Res. Rev.*, **10**, 125–150, https://doi.org/10.1016/j.tcrr.2021.09.002.

Koch, S. E., M. desJardins, and P. J. Kocin, 1983: An interactive Barnes objective map analysis scheme for use with satellite and conventional data. *J. Climate Appl. Meteor.*, **22**, 1487–1503, https://doi.org/10.1175/1520-0450(1983)022<1487:AIBOMA>2.0.CO;2.

Landsea, C. W., and J. L. Franklin, 2013: Atlantic hurricane database uncertainty and presentation of a new database format. *Mon. Wea. Rev.*, **141**, 3576–3592, https://doi.org/10.1175/MWR-D-12-00254.1.

Marchok, T. P., 2002: How the NCEP tropical cyclone tracker works. Preprints, *25th Conf. on Hurricanes and Tropical Meteorology*, San Diego, CA, Amer. Meteor. Soc., P1.13, https://ams.confex.com/ams/pdfpapers/37628.pdf.

——, 2021: Important factors in the tracking of tropical cyclones in operational models. *J. Appl. Meteor. Climatol.*, **60**, 1265–1284, https://doi.org/10.1175/JAMC-D-20-0175.1.

Merrill, R. T., 1987: An experiment in statistical prediction of tropical cyclone intensity change. NOAA Tech. Memo. NWS NHC-34, 37 pp., https://repository.library.noaa.gov/view/noaa/7212.

Mouche, A. A., B. Chapron, B. Zhang, and R. Husson, 2017: Combined co- and cross-polarized SAR measurements under extreme wind conditions. *IEEE Trans. Geosci. Remote Sens.*, **55**, 6746–6755, https://doi.org/10.1109/TGRS.2017.2732508.

——, ——, J. Knaff, Y. Zhao, B. Zhang, and C. Combot, 2019: Copolarized and cross-polarized SAR measurements for high-resolution description of major hurricane wind structures: Application to Irma category 5 hurricane. *J. Geophys. Res. Oceans*, **124**, 3905–3922, https://doi.org/10.1029/2019JC015056.

Mueller, K. J., M. DeMaria, J. Knaff, J. P. Kossin, and T. H. Vonder Haar, 2006: Objective estimation of tropical cyclone wind structure from infrared satellite data. *Wea. Forecasting*, **21**, 990–1005, https://doi.org/10.1175/WAF955.1.

National Hurricane Operations Plan, 2022: NOAA Federal Coordinator Meteorological Services and Supporting Research. Rep. FCM-P12-2022, 186 pp., https://www.weather.gov/media/nws/IHC2022/2022_NHOP_June_1.pdf.

Nolan, D. S., B. D. McNoldy, and J. Yunge, 2021: Evaluation of the surface wind field over land in WRF simulations of Hurricane Wilma (2005). Part I: Model initialization and simulation validation. *Mon. Wea. Rev.*, **149**, 679–695, https://doi.org/10.1175/MWR-D-20-0199.1.

Nordberg, W., J. Conaway, D. B. Ross, and T. Wilheit, 1971: Measurements of microwave emission from a foam-covered, wind-driven sea. *J. Atmos. Sci.*, **28**, 429–435, https://doi.org/10.1175/1520-0469(1971)028%3C0429:MOMEFA%3E2.0.CO;2.

Pasch, R. J., R. Berg, D. R. Roberts, and P. P. Papin, 2021: Tropical cyclone report: Hurricane Laura (20–29 August 2020). NHC Tech. Rep. AL132020, 75 pp., https://www.nhc.noaa.gov/data/tcr/AL132020_Laura.pdf.

Powell, M. D., S. H. Houston, L. R. Amat, and N. Morisseau-Leroy, 1998: The HRD real-time hurricane wind analysis system. *J. Wind Eng. Ind. Aerodyn.* **77–78**, 53–64, https://doi.org/10.1016/S0167-6105(98)00131-7.

——, E. W. Uhlhorn, and J. D. Kepert, 2009: Estimating maximum surface winds from hurricane reconnaissance measurements. *Wea. Forecasting*, **24**, 868–883, https://doi.org/10.1175/2008WAF2007087.1.

——, and Coauthors, 2010: Reconstruction of Hurricane Katrina's wind fields for storm surge and wave hindcasting. *Ocean Eng.*, **37**, 26–36, https://doi.org/10.1016/j.oceaneng.2009.08.014.

Press, W. H., B. P. Flannery, S. A. Teukolsky, and W. T. Vetterling, 1992: *Numerical Recipes in FORTRAN 77: The Art of Scientific Computing*. Cambridge University Press, 1010 pp.

Rappaport, E. N., J.-G. Jiing, C. W. Landsea, S. T. Murillo, and J. L. Franklin, 2012: The joint hurricane test bed: Its first decade of tropical cyclone research-to-operations activities reviewed. *Bull. Amer. Meteor. Soc.*, **93**, 371–380, https://doi.org/10.1175/BAMS-D-11-00037.1.

Rogers, R., S. Lorsolo, P. Reasor, J. Gamache, and F. Marks, 2012: Multiscale analysis of tropical cyclone kinematic structure from airborne Doppler radar composites. *Mon. Wea. Rev.*, **140**, 77–99, https://doi.org/10.1175/MWR-D-10-05075.1.

Sampson, C. R., and A. J. Schrader, 2000: The Automated Tropical Cyclone Forecasting System (version 3.2). *Bull. Amer. Meteor. Soc.*, **81**, 1231–1240, https://doi.org/10.1175/1520-0477(2000)081<1231:TATCFS>2.3.CO;2.

——, and J. A. Knaff, 2015: A consensus forecast for tropical cyclone gale wind radii. *Wea. Forecasting*, **30**, 1397–1403, https://doi.org/10.1175/WAF-D-15-0009.1.

——, E. M. Fukada, J. A. Knaff, B. R. Strahl, M. J. Brennan, and T. Marchok, 2017: Tropical cyclone gale wind radii estimates for the western North Pacific. *Wea. Forecasting*, **32**, 1029–1040, https://doi.org/10.1175/WAF-D-16-0196.1.

——, J. S. Goerss, J. A. Knaff, B. R. Strahl, E. M. Fukada, and E. A. Serra, 2018: Tropical cyclone gale wind radii estimates, forecasts, and error forecast for the western North Pacific. *Wea. Forecasting*, **33**, 1081–1092, https://doi.org/10.1175/WAF-D-17-0153.1.

Sapp, J. W., S. O. Alsweiss, Z. Jelenak, P. S. Chang, and J. Carswell, 2019: Stepped frequency microwave radiometer wind-speed retrieval improvements. *Remote Sens.*, **11**, 214, https://doi.org/10.3390/rs11030214.

Schwerdt, R. W., F. P. Ho, and R. W. Watkins, 1979: Meteorological criteria for standard project hurricane and probable maximum hurricane wind fields, Gulf and East Coasts of the United States. NOAA Tech. Rep. NWS 23, 356 pp., https://repository.library.noaa.gov/view/noaa/6948/noaa_6948_DS1.pdf.

Thacker, W. C., 1988: Fitting models to inadequate data by enforcing spatial and temporal smoothness. *J. Geophys. Res.*, **93**, 10 655–10 665, https://doi.org/10.1029/JC093iC09p10655.

Torn, R. D., and C. Snyder, 2012: Uncertainty of tropical cyclone best-track information. *Wea. Forecasting*, **27**, 715–729, https://doi.org/10.1175/WAF-D-11-00085.1.

Uhlhorn, E. W., and P. G. Black, 2003: Verification of remotely sensed sea surface winds in hurricanes. *J. Atmos. Oceanic Technol.*, **20**, 99–116, https://doi.org/10.1175/1520-0426(2003)020<0099:VORSSS>2.0.CO;2.

——, and D. S. Nolan, 2012: Observational undersampling in tropical cyclones and implications for estimated intensity. *Mon. Wea. Rev.*, **140**, 825–840, https://doi.org/10.1175/MWR-D-11-00073.1.

——, P. G. Black, J. L. Franklin, M. Goodberlet, J. Carswell, and A. S. Goldstein, 2007: Hurricane surface wind measurements from an operational stepped frequency microwave radiometer. *Mon. Wea. Rev.*, **135**, 3070–3085, https://doi.org/10.1175/MWR3454.1.

——, B. W. Klotz, T. Vukicevic, P. D. Reasor, and R. F. Rogers, 2014: Observed hurricane wind speed asymmetries and

relationships to motion and environmental shear. *Mon. Wea. Rev.*, **142**, 1290–1311, https://doi.org/10.1175/MWR-D-13-00249.1.

Willoughby, H. E., and M. E. Rahn, 2004: Parametric representation of the primary hurricane vortex. Part I: Observations and evaluation of the Holland (1980) model. *Mon. Wea. Rev.*, **132**, 3033–3048, https://doi.org/10.1175/MWR2831.1.

Zhang, J. A., and E. W. Uhlhorn, 2012: Hurricane sea surface inflow angle and an observation-based parametric model. *Mon. Wea. Rev.*, **140**, 3587–3605, https://doi.org/10.1175/MWR-D-11-00339.1.